APPLIED SCIENCES AND ENGINEERING

Dynamic thermal trapping enables cross-species smart nanoparticle swarms

Tongtao Li[1], Kwok Hoe Chan[1], Tianpeng Ding[1], Xiao-Qiao Wang[1], Yin Cheng[1], Chen Zhang[1], Wanheng Lu[1], Gamze Yilmaz[1], Cheng-Wei Qiu[1]*, Ghim Wei Ho[1,2,3]*

Bioinspired nano/microswarm enables fascinating collective controllability beyond the abilities of the constituent individuals, yet almost invariably, the composed units are of single species. Advancing such swarm technologies poses a grand challenge in synchronous mass manipulation of multimaterials that hold different physiochemical identities. Here, we present a dynamic thermal trapping strategy using thermoresponsive-based magnetic smart nanoparticles as host species to reversibly trap and couple given nonmagnetic entities in aqueous surroundings, enabling cross-species smart nanoparticle swarms (SMARS). Such trapping process endows unaddressable nonmagnetic species with efficient thermo-switchable magnetic response, which determines SMARS' cross-species synchronized maneuverability. Benefiting from collective merits of hybrid components, SMARS can be configured into specific smart modules spanning from chain, vesicle, droplet, to ionic module, which can implement localized or distributed functions that are single-species unachievable. Our methodology allows dynamic multimaterials integration despite the odds of their intrinsic identities to conceive distinctive structures and functions.

INTRODUCTION

Natural collectivity, such as fish schooling, can achieve a wide range of cooperative patterns and motions by coordinating simple individuals (*1*). Mimicking such behavior promises exciting opportunities in emerging areas at the interface of nanoscience and intelligent technologies (*2*), while the key to reproducing such capabilities lies in how to control and couple discrete artificial entities (*3*), especially in fluidic environments (*4*). To date, burgeoning efforts have been devoted to devise methodologies to manipulate objects (*5*–*9*), among which optical trapping represents a highly versatile technique enabling robust manipulation of micro/nanoscale species (*10*). Nevertheless, this otherwise promising technique suffers from restrictions including lack of efficiency and large-area synchronized manipulation incapability (*11*). By contrast, conventional solvent evaporation allows scale-up assembly of colloidal nanoparticles (NPs) (*12*, *13*), yet structural reconfigurability of the ensembles is restricted (*14*).

Alternate approaches that can potentially surmount the above-mentioned limitations have also been explored in recent years (*15*–*18*). In this respect, magnetic-based manipulation exemplifies an attractive pathway to fulfill the high-efficiency dynamic control and parallel manipulation (*19*). Over the past decades, numerous techniques have been developed by using the magnetic-related manipulation behaviors, leading to a set of advances in diverse areas such as material synthesis, biomedicine, microfluidics, and soft robotics (*20*). However, apart from various established advantages (*21*, *22*), most existing strategies are either constrained in operating conditions (e.g., require patterned surface) or invariable in materials applicability (dedicated to magnetic materials). Meanwhile, thermal stimulus that can be remotely activated, in a noninvasive and suspended manner (*23*), as well as easily coupled with other response (*24*), provides another possibility for scalable manipulability. A myriad of dynamic functional materials and systems based on thermal response have been developed (*25*). However, unlike the thriving progresses on the bulk scale demonstrations (*26*, *27*), the development of swarm control of miniaturized (micro- to nanoscale) counterparts is sluggish despite the initial advances (*28*, *29*). Furthermore, almost all the current miniaturized systems are constrained to elementary control (such as simple dynamic aggregation) of a single species, typically translating into limited functionalities and applications (*30*, *31*). On the other hand, hybrid aggregation of different materials at aqueous medium is not unexpected in chemistry and materials science (*32*, *33*), yet their common consequences are partial aggregation or severe phase separation (*34*), and the high-efficiency dynamic manipulations are even more challenging. To our knowledge, little headway to date has been made in the dynamically synchronous manipulation of independent, cross-species objects in aqueous environment, against the odds of intrinsic differences (in terms of components, physicochemical properties, and dimensions, among others) of dissimilar species and high-fluidity matrixes.

Here, the challenge of collective bridging of dissimilar species into an autonomous controlled system is overcome by a dynamic thermal trapping strategy, enabled by cross-species smart NP swarms (termed SMARS). SMARS are composed of host magnetic NP (MNP) species capped with thermoresponsive polymer and customizable nonmagnetic trapped species (Fig. 1A). The trapping process imparts SMARS with reversible and synchronized maneuverability of dissimilar entities that are originally perceived as spatially nonaddressable. The key capabilities of SMARS lie in the host magnetic particles capable of almost 100% trapping and manipulating of nonmagnetic foreign species that outsize and outnumber several times the host in an aqueous environment. Furthermore, SMARS are endowed with reconfigurability and modularity, given its collective merits of accessibility to individual entity and the fluidic deformability. SMARS can be readily reconfigured into single-species unachievable functional smart modules that span from chain, vesicle, droplet, to ionic module to implement localized (e.g., actuation, shape morphing,

[1]Department of Electrical and Computer Engineering, National University of Singapore, 4 Engineering Drive 3, Singapore 117583, Singapore. [2]Department of Materials Science and Engineering, National University of Singapore, 9 Engineering Drive 1, Singapore 117575, Singapore. [3]Institute of Materials Research and Engineering, A*STAR (Agency for Science, Technology and Research), 3 Research Link, Singapore 117602, Singapore. *Corresponding author. Email: chengwei.qiu@nus.edu.sg (C.-W.Q.); elehgw@nus.edu.sg (G.W.H.)

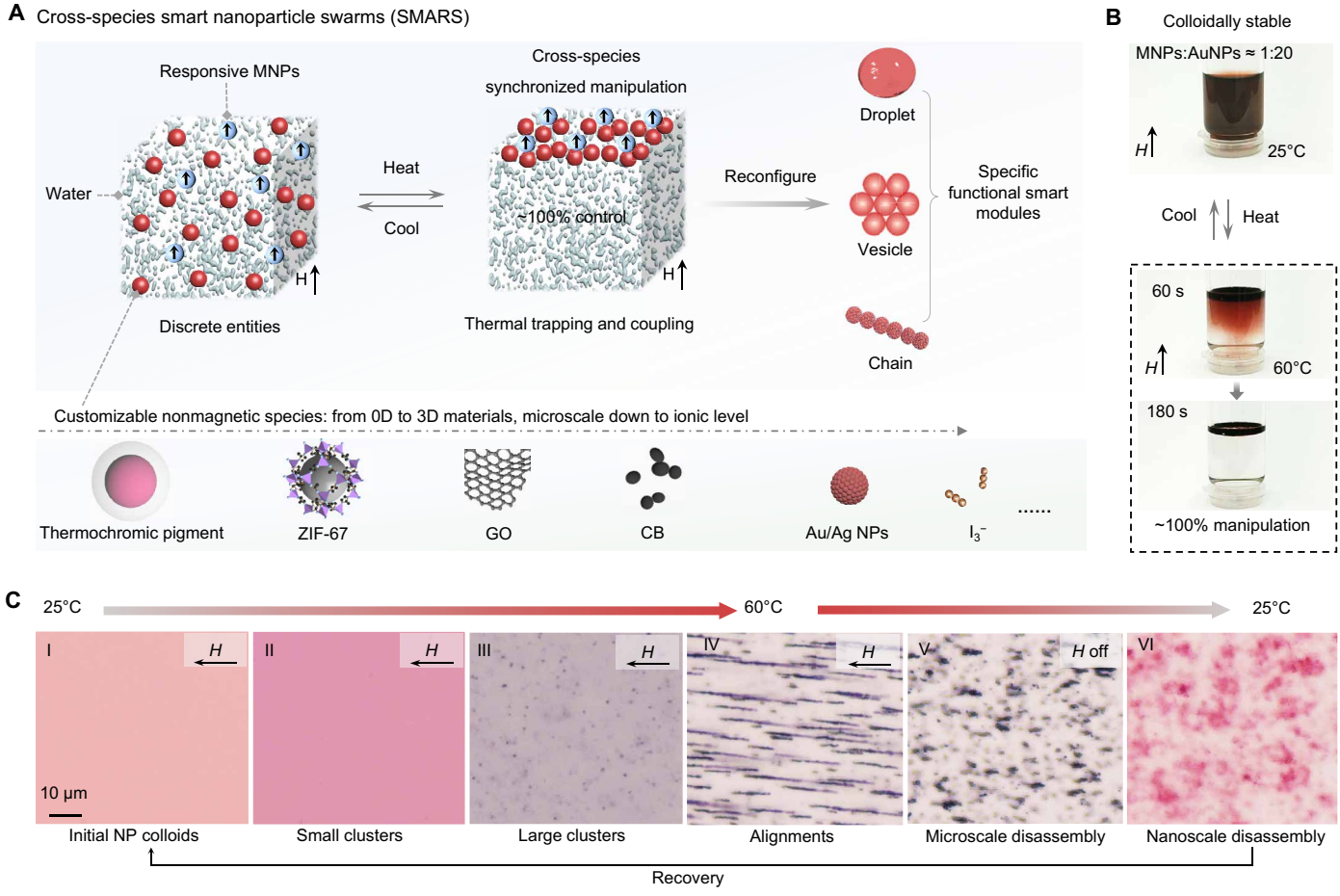

Fig. 1. General concept of SMARS and its cross-species synchronized maneuverability. (**A**) Schematic illustrations of the SMARS, displaying the collective behaviors, reconfigurability, and multimaterial manipulation. (**B**) Photographs of exemplified SMARS (taking ~14-nm AuNPs as trapped entities, with a mass ratio of MNPs:AuNPs ≈ 1:20), indicating the thermal switchable trapping and ~100% magnetic manipulation of nonmagnetic AuNPs. (**C**) Snapshots of SMARS revealing a temperature-dependent closed-loop process for the dynamic trapping and manipulation of AuNPs from initial colloidal NP solution (I), to small clusters (II), large clusters (III), alignment (IV), microscale disassembly (V), nanoscale disassembly (VI), and recovery stage. Photo credit: Tongtao Li, National University of Singapore.

transport, and separation) or distributed functions [e.g., remotely regulating transmittance and thermoelectric (TE) performance].

RESULTS

Observation of the cross-species synchronized manipulation of SMARS

Figure 1B shows the representative SMARS with ~14-nm gold NPs (AuNPs; bright red) as trapped species. SMARS retain a nonaddressable colloidal state at 25°C, even with the prolonged exposure to magnetic field (*H*) of several weeks, owing to the energetic random Brownian motion. However, at otherwise identical conditions, a higher temperature (60°C) results in almost 100% magnetic manipulation of both ~10-nm MNPs and nonaddressable nonmagnetic AuNPs, as shown by the distinct solution color change and particle swarming locomotion in Fig. 1B and fig. S1. This phenomenon is not just remarkable, but what makes it more impactful is the facile preparation of SMARS, which makes them feasible for practical applications. In a typical preparation of SMARS, poly(*N*-isopropylacrylamide) (pNIPAM), a very common thermal responsive polymer with mild coil-to-globule temperature (T_c = 32°C), was selected as a ligand to engineer the surface of AuNPs and MNPs by a ligand exchange process (Materials and Methods and figs. S2 and S3). The key construction feature of SMARS lies in the rational modulation of the polymer concentration capped on MNPs and AuNPs. Direct mixing the two kinds of prepared species, with a user-specific particle mass ratio (e.g., MNPs:AuNPs ≈ 1:20), leads to SMARS. Such a simple yet unusual surface concentration control methodology not only easily defines the host (high concentration) and trapped (low concentration) species but also determines the aggregation hydrodynamics during phase transition to enable a high-efficiency cross-species synchronized manipulation.

To further observe and elucidate the thermo-switchable magnetic maneuverability of SMARS, we used an optical microscope attached with an external magnetic field and heater to monitor the process. The dynamic evolution of SMARS, which proceeds from the initial colloidal stable solution (I) to small cluster (II), large cluster (III), microchain alignments (IV), microscale disassembly (V), nanoscale disassembly (VI), and recovery stage, was clearly manifested within a cyclic temperature of ~25° to 60°C (Fig. 1C, fig. S4, and movie S1).

While phase transition and trapping behaviors occur at stage II, the cluster size is still too small to allow the effective magnetic control because of intense Brownian motion. As the formation of large clusters (III and IV) transpires, magnetic manipulation is activated as the magnetic force becomes dominant (fig. S5), leading to the swarming of the microparticles into microchain alignments. At stage V, when H is off, such long microchain alignments are disassembled into independent microparticles. Attributed to the strong elastic interparticle repulsion of SMARS when $T < T_c$, both thermal and magnetic fields do not result in irreversible aggregation (VI). Likewise, controlling SMARS by temperature only generates a similar reversible process, except for the absence of alignment stage that is attributed to a magnetic manipulation behavior (fig. S6). The contrasting color changes at different stages arise from the changes in interparticle spacing of AuNPs, induced by the collapse or recovery of pNIPAM under different temperatures (fig. S7). Besides, SMARS also reveal an excellent thermal stability at a wide range of temperature (e.g., −20° to 90°C), as shown in fig. S8.This further validates the effective trapping and remarkable maneuverability of the SMARS that capitalize magnetic host species to adeptly manipulate non–magnetic-trapped species.

The thermal trapping mechanism and versatility of SMARS

As described earlier, we found that the intriguing trapping and manipulating behaviors are highly dependent on the surface concentration (ψ) modulation of pNIPAM capped on the host and trapped species. The ψ can be estimated by the equation $\psi = N_{pNIPAM}/SA_{NP}$, where N_{pNIPAM} is the pNIPAM number on a single NP and SA_{NP} is the surface area of a single NP (see Supplementary note 1). To identify the trapping mechanism, we conduct a series of crossover experiments (figs. S9 and S10 and table S1) to deliberately investigate the dependence of the synchronized manipulating behaviors of SMARS on the pNIPAM coverages of MNPs (ψ_{MNP}) and AuNPs (ψ_{AuNP}). The summarized color-scaled diagram (Fig. 2A) clearly reveals the distinct differences in the magnetic controllability of SMARS with the variation of ψ_{AuNP} and ψ_{MNP}. Not unexpectedly, insufficient pNIPAM coverages of host MNPs, such as $\psi_{MNP} \approx 0.02$, 0.10, and 0.52/nm^2, result in partial manipulation of constituent particles in SMARS, while increasing ψ_{AuNP} contributes to the augmentation of the control efficiency. This is because low ψ_{MNP} signifies weak hydrophobicity when $T > T_c$, which is unable to undertake the "host" role of MNPs to effectively trap the nonmagnetic AuNPs and thus leads to an inadequate magnetic control of the overall system. When it comes to SMARS with higher ψ_{MNP} (e.g., $\psi_{MNP} \approx 1.04$, 1.56, and 2.08/nm^2), the unexpected moderate ψ_{AuNP} rather than its higher counterparts enables the best cross-species magnetic controllability (~100%). To specifically elucidate such phenomenon, we take three representative SMARS with identical ψ_{MNP} (2.08/nm^2) yet different ψ_{AuNP} as examples (Fig. 2B). Clearly, when $\psi_{AuNP} \approx 0.02$/nm^2, only a fraction (~33%) of the total particles (estimated by the particle concentration changes in solution) can be manipulated by magnetic fields, while such ratio can reach to ~100% at $\psi_{AuNP} \approx 0.13$/nm^2 (table S1). A higher concentration on AuNPs ($\psi_{AuNP} \approx 2.6$/nm^2) leads to obvious particle residues (~19%) that were failed to be manipulated (Fig. 2B and table S1), validating that the higher concentration of responsive polymer does not mean better magnetic maneuverability of SMARS. Figure 2C shows scanning electron microscopy (SEM) images taken from different SMARS in Fig. 2B by immobilizing the alignment stage on a silica surface. The SEM images indicate that the aggregation size and uncontrolled particle ratios of the SMARS depend on the ψ_{AuNP} when fixing ψ_{MNP} (2.08/nm^2). It is clear that the higher ψ_{AuNP} leads to larger aggregations, whereas the moderate ψ_{AuNP} case (0.13/nm^2) reveals minimum particle residues, that is, the optimal magnetic maneuverability.

All these results disclose that the rational modulation of surface polymer concentration between MNPs and AuNPs is crucial for the effective synchronous manipulation. First, MNPs with relatively adequate pNIPAM are pivotal to guarantee their role as hosts to realize efficient trapping of nonmagnetic AuNPs and synchronized magnetic manipulation, which is expected. Second, in cases of sufficient ψ_{MNP}, differentiation of ligand concentration on MNPs and AuNPs, which renders different phase behaviors of such two-type particles, leads to the dynamic, almost 100% maneuverability of SMARS (Fig. 2D). Specifically, when $\psi_{AuNP} << \psi_{MNP}$ (e.g., the left picture in Fig. 2B), although MMPs can rapidly form numerous hydrophobic trap centers when heated up, the AuNPs are still ineffectively trapped because of its weak hydrophobicity. Increasing the ψ of AuNPs while keeping $\psi_{AuNP} < \psi_{MNP}$ produces another kind of trapping and manipulation behaviors. In particular, when system temperature changes from $T < T_c$ to $T > T_c$, the MNPs preferentially become hydrophobic owing to its high pNIPAM concentration, which then simultaneously trap the hydrophobic AuNPs into sizeable clusters to facilitate almost 100% magnetic manipulation of the nonmagnetic AuNPs that is initially uncontrollable. Such a trapping behavior can guarantee that each cluster contains MNP species to enable effectual magnetic manipulation. Further increasing ψ of AuNPs to $\psi_{AuNP} \geq \psi_{MNP}$ weakens the manipulation behavior. We surmise that this unexpected phenomenon is ascribed to the loss of preferential trapping behavior because of the comparable phase transition capabilities between nonmagnetic AuNPs and MNPs. In such cases, although the formation of large aggregation may facilitate magnetic manipulation, it is accompanied by a portion of particle clusters whose MNP ratio is too low to enable effective magnetic manipulation. For contrasting illustrations, SMARS composed of various ratios of MNPs were prepared to show that higher MNP ratio leads to better controllability while preserving differentiated control behaviors of different ligand concentration cases, as shown in fig. S11. This not only illustrates that the particle ratio represents another key factor to regulate the manipulating behaviors but also corroborates the formation of uncontrollable low-magnetic clusters at high polymer coverage. Although more magnetic species can bring forth an enhanced magnetic maneuverability, it also means a severe loss of trapped species with unique features that are host particles is unachievable, which is a main advantage of SMARS. This definitely highlights the essentiality of the ψ differentiation for the highly efficient cross-species trapping as well as maximizes the collective performances of different materials. Here, we emphasize that the ~100% controllability of SMARS highly merits its further functions, as poor or low-efficiency controllability usually limits or renders useless applications.

On the basis of similar mechanism, diverse SMARS with various trapped materials of different dimensions and physiochemical properties are readily constructed. As shown in Fig. 2E and fig. S12, different unaddressable nonmagnetic materials are aligned, such as silver NPs (AgNPs), carbon black (CB), graphene oxide (GO), zeolitic imidazolate framework-67 (ZIF-67), and thermochromic pigment (TCP), validating successful trapping and manipulation. SMARS enable building of complex structural materials by introducing

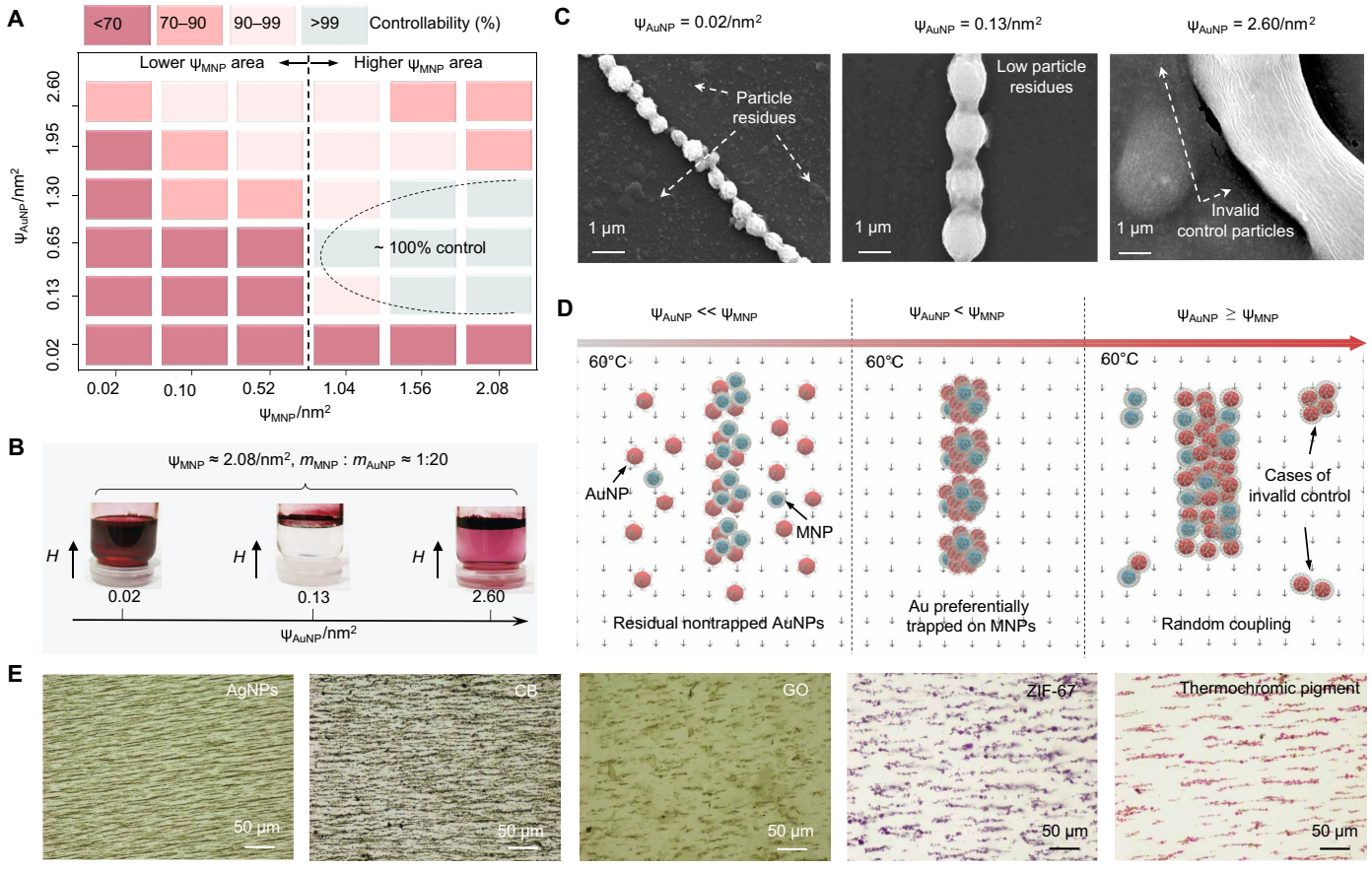

Fig. 2. Dynamic thermal trapping mechanism and versatility of SMARS. (**A**) Color-scaled diagram showing the diverse magnetic controllability of SMARS with the variation of ψ_{AuNP} and ψ_{MNP}. The mass ratio of MNP:AuNP is fixed to 1:20. (**B**) Photographs of three representative SMARS after exposure to magnetic field at 60°C, distinctly presenting the differences in cross-species maneuverability for SMARS with different surface coverages of pNIPAM on MNPs and AuNPs.(**C**) SEM images of SMARS with $\psi_{AuNP} \approx 0.02$, 0.13, and 2.6/nm^2, respectively, indicating that ψ_{AuNP} distinctly influences the aggregation size and uncontrolled particle ratio at otherwise identical conditions. (**D**) Schemes showing the modulation of ψ on MNPs and AuNPs are crucial for the effective cross-species synchronized maneuverability of SMARS. (**E**) Optical microscopy (OM) images taken at alignment stage of various SMARS with AgNPs, CB, GO, ZIF-67, and TCP as trapped materials, respectively, showing the generality of the dynamic thermal trapping strategy. Photo credit: Tongtao Li, National University of Singapore.

different trapped species, which otherwise are not easily available, such as Au-Fe_3O_4, Ag-Fe_3O_4 microchains (Au-Ag-FMCs), by mixing two-type SMARS with AuNPs and AgNPs as trapped species, respectively (fig. S13).

Microscale shape-color-change SMARS chain actuator (chain module)

In contrast to the reversible process from NP to microchain alignments discussed earlier, the interception and encapsulation of a node/section at the dynamic "microchain" stage (Fig. 1C, IV) result in "chain module" SMARS that induce unusual "finite/confined" reconfigurable behavior (Fig. 3, A and B). Leveraging on the synergic integration of magnetic and plasmonic species alongside conformal encapsulation, the SMARS chains embrace superiorities in persistent chain-like structure in both hot and cool water (fig. S14), demonstrating (opto)thermal-dependent color-morphological changes and magnetic actuation. To investigate whether the thermoresponsive properties associated with the PNIPAM is still active/vibrant after encapsulation, we heated aqueous suspension comprising SMARS microchains above the T_c of PNIPAM and monitored the (opto) thermal-dependent changes using microscopy in bright-field mode (Fig. 3C and movie S2). The SMARS chain underwent reversible transformation of color change and representative length shrinkage up to 20% at 60°C of almost 100% recoverability (Fig. 3D). It should be emphasized that the structural transformation of the SMARS chains is highly reproducible, as shown in the cyclic heating/cooling from ~25° to 60°C in Fig. 3E. The atomic force microscopy (AFM) image shows a naturally dried SMARS chain on a silica at room temperature, which corroborates with an earlier synthetic description of SMARS microparticles containing numerous NPs (Fig. 3F). Furthermore, the height profile analysis reveals that the dried microparticles of SMARS chain are almost flat (Fig. 3G), which substantiates the formation of a thin conformal shell enclosing freely distributed NP swarms. In addition to the ingenious reversible color changes and volume/length evolution, a selected "L-shape" SMARS chain, which can be prepared by a simple two-step magnetic field control route (fig. S15), verifies effectual magnetic actuation behavior. Note that although magnetic response is very common, harnessing magnetic field to control a freestanding hybrid microactuator whose mass of nonmagnetic AuNPs is 20 times that of magnetic materials has not been available. By exerting different external magnetic stimuli, a relevant response can be produced, such as 360° rotation (Fig. 3H

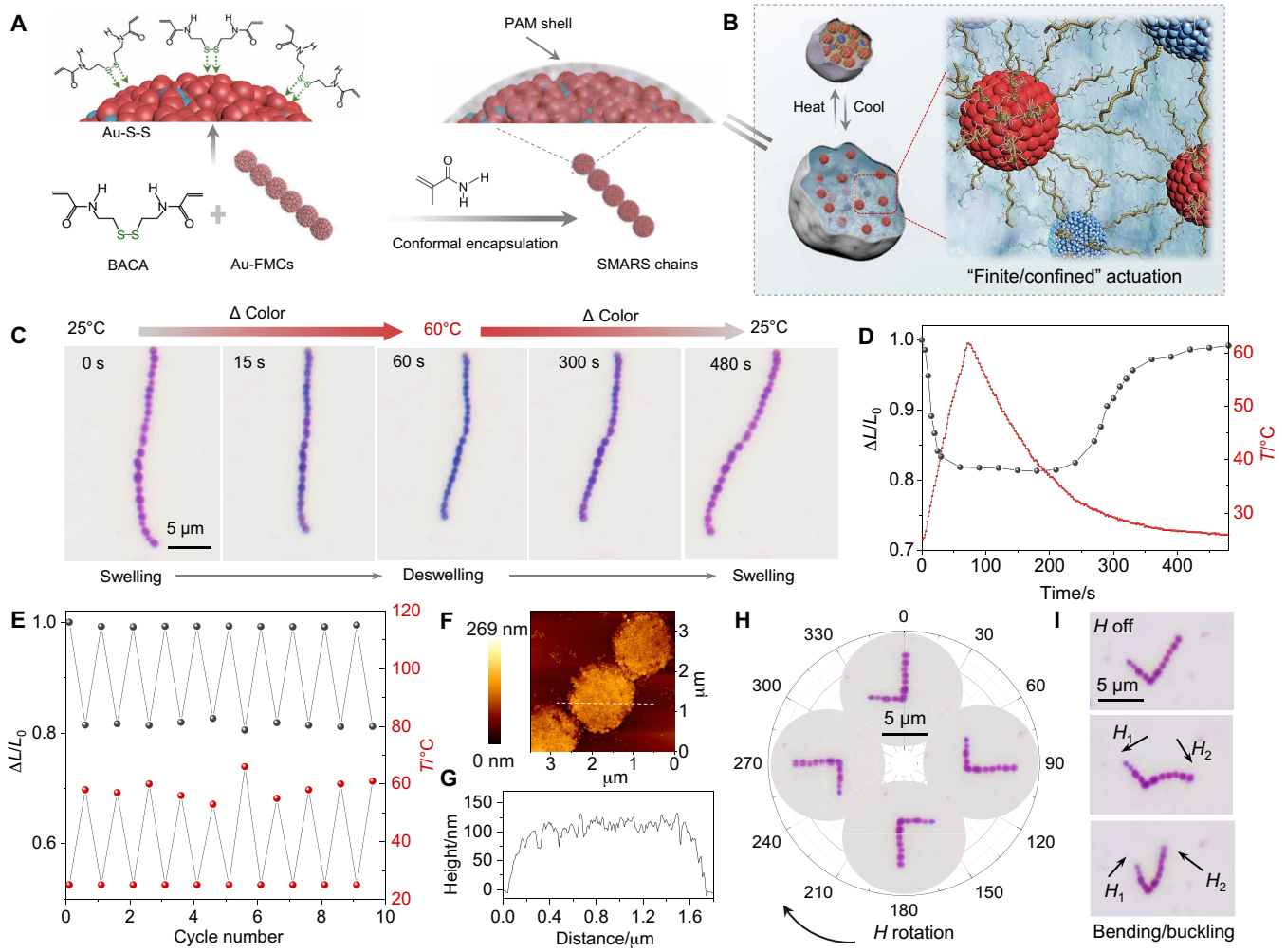

Fig. 3. SMARS microchain with chameleon-like actuation (chain module). (**A**) Schematic formation of a conformal hydrogel shell with the trapped AuNP active site to absorb BACA cross-linker in the in situ free radical polymerization. (**B**) Schematic illustration for the dynamic process of the chameleon-like SMARS. Taking advantage of the Au-thiolate interaction from the trapped AuNPs of SMARS, using BACA as a cross-linker, a nanoscale conformal encapsulation of Au-Fe_3O_4 microchains with polyacrylamide (PAM) has been judiciously realized, leading to otherwise inaccessible chameleon-like SMARS chain module. (**C**) Representative OM images showing temperature-dependent changes of color, volume, and length. Changes of length $\Delta L/L_0$ and temperature T as a function of time (**D**) and cycle number (**E**). (**F**) AFM image of representative chameleon-like SMARS naturally drying on a cleaned silica at 25°C. (**G**) A height profile across the white dotted line in (F) showing a flat feature of the composed cluster, further substantiating the formation of thin PAM shell enclosing freely distributed NPs. Unique L-shape chains displaying the 360° rotation (**H**) and deformation of the chameleon-like SMARS (**I**).

and movie S3), bending, or buckling deformation (Fig. 3I and movie S4). Other than a single freestanding SMARS chain exposition, an array of one-end anchored SMARS chains presents a seagrass-like synchronic microactuation (fig. S16).

Multiple reconfigurable, SWL-controlled SMARS vesicles (vesicle module)

The reconfigurability of SMARS embraces not only the dynamic manipulation of contained species and selective encapsulation of a dynamic course but also subsumes remarkable fluidic deformability of the overall system. When directly emulsifying SMARS in a nonpolar solvent using maleic copolymer as surfactants (see Materials and Methods and fig. S17), SMARS vesicles (tens of micrometer to millimeter scale) with multiscale reconfigurability emerges. Starting from spherical SMARS vesicles at room temperature (Fig. 4A, i), simultaneously exerting magnetic and thermal fields induces dynamic assembly and swarming locomotion of contained particles, which leads to interior reconfiguration from non-Janus to Janus spherical structures accompanied by temperature-dependent color changes [Fig. 4A (ii to v) and movie S5]. When magnetic field and heat are suspended, natural diffusion of NPs at room temperature drives the Janus spherical SMARS vesicles back to its initial state. On the other hand, evaporation of surrounding nonpolar solvent of SMARS vesicles results in the exterior shape reconfiguration from sphere to polyhedron with distinct boundary (fig. S18) in both Janus and non-Janus interior structures and vice versa (movies S6 and S7). Likewise, a similar Janus–to–non-Janus evolution to that of spherical ones was also observed in polyhedral vesicles. Controlled combinatorial evaporation and thermomagnetic stimuli allow one to continuously attain synchronous multiscale reconfigurability [Fig. 4A (vi to x) and movie

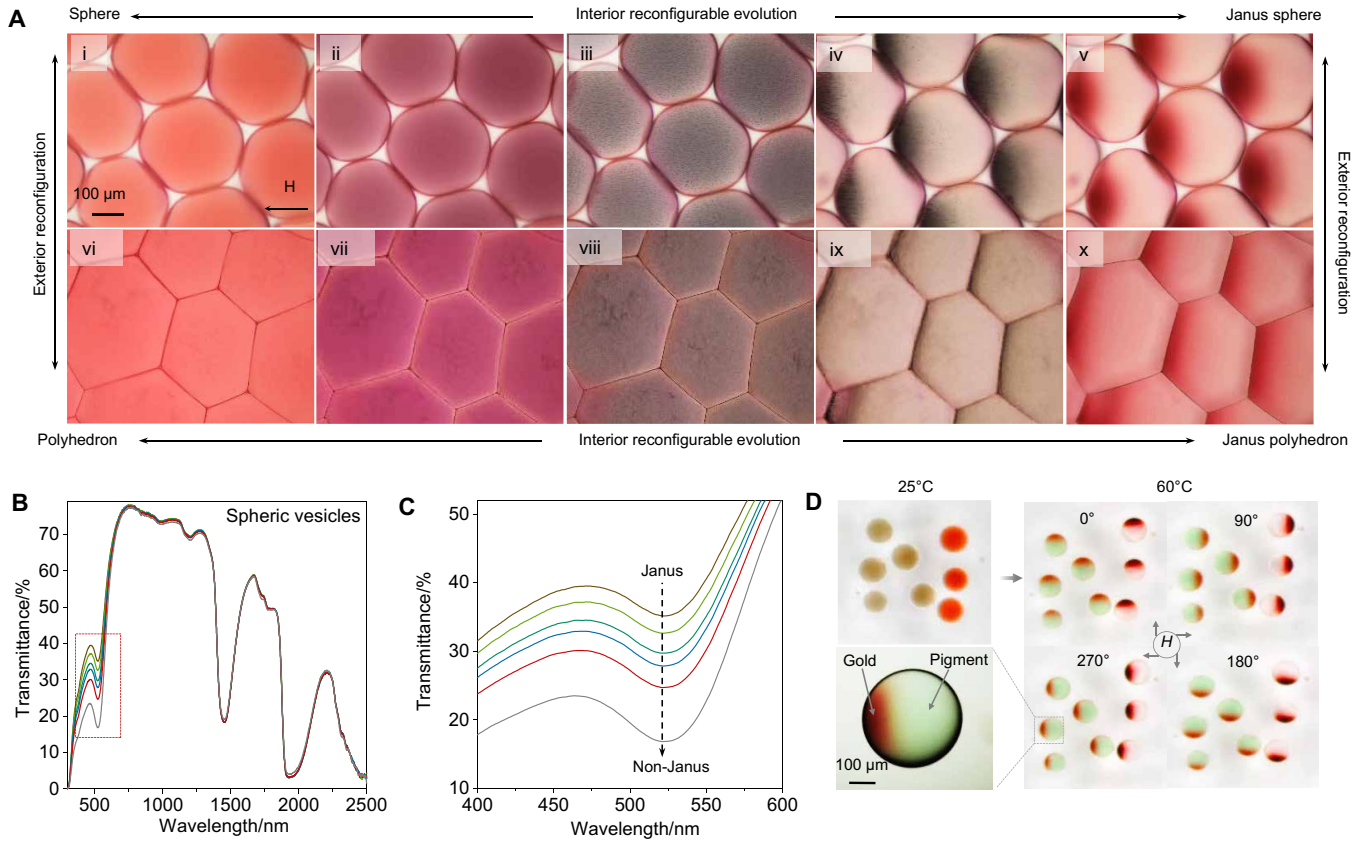

Fig. 4. SMARS vesicles with multiscale reconfigurability and controllability of SWL transmittance (vesicle module). (**A**) Representative OM images of SMARS vesicles showing both exterior (macroscale) and interior (nano- to microscale) reconfigurations, accompanied by color changes. (**B**) In situ full-wavelength transmittance spectra of monolayer spherical SMARS vesicles showing the transformation from Janus to non-Janus interior structures. (**C**) A zoom-in of the region indicated in (B). (**D**) OM images of an "N"-shape system containing two kinds of independent vesicles. The brown vesicles at 25°C are multiple-component SMARS composed of red AuNPs, green pigment, and MNPs, while the red one is Au-SMARS, showing simultaneously the selective manipulation of different species and interior 360° locomotion.

S8]. Specifically, by virtue of the reconfigurability and maneuverability, the AuNPs can be readily and deterministically relocated, making the SMARS vesicles available to control the transmittance of specific wavelength light (SWL) (fig. S19). The shape and packing structure of SMARS vesicles can be specified by the content of a nonpolar solvent, enabling a wider spectral modulation (fig. S20). The interior evolution of both spherical (Fig. 4, B and C) and polyhedral (fig. S21, A and B) SMARS vesicles at room temperature, from Janus to non-Janus structures, are investigated by the transmittance spectra, showing a distinct controllability of SWL (e.g., 524 nm) transmittance (from 37 to 18%). Except for the wavelength in the range of ~400 to 600 nm, all the other regions remain invariant during structural evolution, signifying the controllability of SWL resulting from the interior spatial adaptations of the AuNP-containing SMARS vesicles. Figure S21C presents the optical modulation ranges at different wavelengths (e.g., 470 and 524 nm) in accordance with exterior shape and packing structure alterations. Given the flexibility of preparing SMARS vesicles, one can easily tailor the broadness and selectivity of the modulation ranges of light transmittance by changing the size or constituents of vesicles. Although controlled light absorption at different wavelengths for AuNPs is well known (as also seen in Figs. 1C and 3C), the active controllable transmission of SWL capitalizing on the dynamic NP locomotion within the same system has not been reported. In addition, diverse interior switchable swarming behaviors, such as 360° transportation (fig. S22) and selective manipulation of specific species in multicomponent vesicle, were also demonstrated. Specifically, only gold particles (red) were locomoted and rotated, selectively leaving the unconditioned pigment materials (green) behind (Fig. 4D), which promise more possibilities of these SMARS vesicles.

Macroscopic SMARS droplet transporter (droplet module)

Furthermore, continuous enlargement of the SMARS geometry enables yet another intriguing variant, that is, SMARS droplet. It is widely known that the use of the magnetic field to guide the locomotion of small-volume droplet–containing magnetic materials, reminiscent of ferrofluids (FFs), is a common but powerful way to modulate the droplet itself or other cargos in an open environment (*21*, *35*). However, it is challenging to separate the solute particles (e.g., MNPs) from the solvent (e.g., water) for the conventional FFs because of the strong MNP-water interactions, hindering further applications. In contrast, other magnetic actuation strategies, such as "liquid marble" or droplet comprising phase-separated MNPs (*36*, *37*), afford controlled solute/solvent separation, but the manipulability is discounted relative to FFs. A SMARS droplet with smart hierarchical operability rightly circumvents the above-mentioned limitations,

capable of not only robust long-distance directional transportation but also localized solute/solvent separation in a designated location triggered by (opto)thermal stimuli (Fig. 5A). Such attributes of the SMARS droplet provide a powerful pathway to quickly transport water over ultralong distances on a complex superhydrophobic surface (fig. S23). Furthermore, the separated particle "solute" is recyclable, which can be readily redispersed into pure water at low temperature, making continued water transport available. As shown in Fig. 5B and movie S9, at room temperature, the SMARS droplet reveals 360° maneuverability on an open superhydrophobic surface (~15 cm), disclosing superb colloidal stability even under magnetic fields (fig. S24). Particularly, when transporting a SMARS droplet to a specific location and triggering the AuNP trapping and cluster formation by (opto)thermal stimuli (where $T > T_c$), both the trapped AuNPs and host MNPs can be thoroughly separated from the SMARS droplet, yielding clean water droplet (fig. S25). To gain a deeper insight into the separation process, we closely monitored the process (movie S10). Figure 5C and fig. S26 show an overview of the separation process. At $T < T_c$, the SMARS droplet maintains a colloidal state (stage I); when under the influence of the magnetic field (H_1, ~157 Oe) and rapid heating, interior separation is induced, where the AuNPs and host MNPs were collectively swarming into a "jacket"

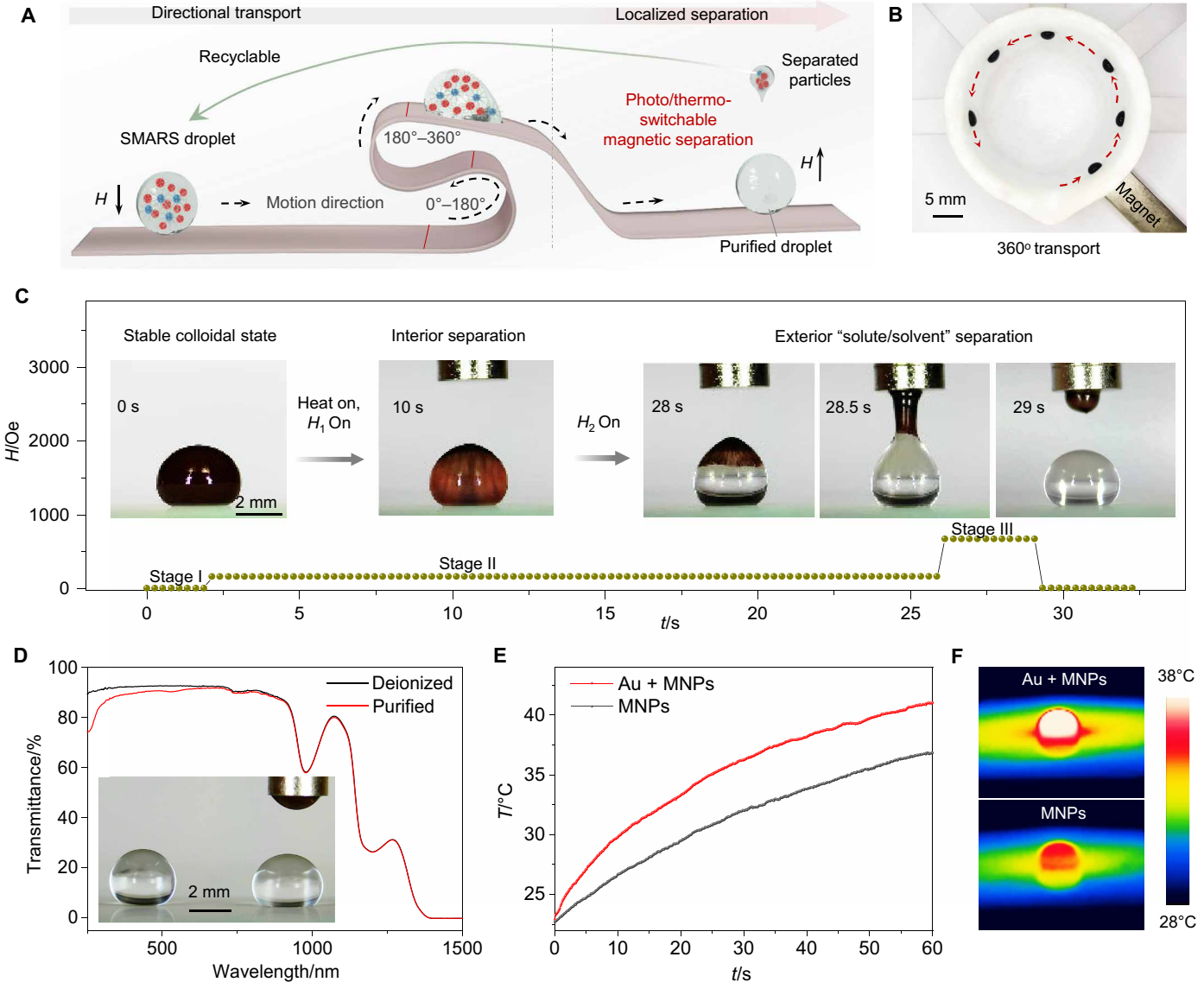

Fig. 5. SMARS droplet with arbitrary surface water transport and localized separation (droplet module). (**A**) Schematic illustration of the hierarchical manipulation concept. (**B**) Superposed frames indicating the tracking on a 360° superhydrophobic surface, which can be divided into flat, inclined, vertical, and even upside down, highlighting the excellent transport ability of FF-like droplets. (**C**) OM images of SMARS droplet showing the thermo-switchable separation process under different magnetic field. (**D**) Transmittance comparison of purified water and controlled DI water, indicating high efficiency of separation. Inset is a representative photograph of separated droplet and DI water droplet. (**E**) Temperature evolution profiles of SMARS droplet [MNPs:Au =1:20, mass/mass (*m*/*m*)] and MNP droplet (MNPs:Au =1:0, *m*/*m*) with similar concentration under simulated five sun intensity irradiation by a xenon lamp. (**F**) The corresponding infrared images after 60 s, suggesting that the SMARS droplet with high proportion of plasmonic AuNPs warrants superior photothermal conversion. Photo credit: Kwok Hoe Chan, National University of Singapore.

layer on the interface of the SMARS droplet, presumably due to a lower polarity of the surface (stage II). At a stronger magnetic field (H_2, ~670 Oe), the exterior separation is stimulated (stage III), analogous to stripping off the jacket, resulting in a purified water droplet and recovered NPs (host and trapped species). The purity of the droplet has been ascertained by transmittance characterizations and optical images, as shown in Fig. 5D, both of which are comparable to the control pure water specimen. In the absence of a thermal stimulus, it should be noted that light source can alternatively be used to achieve a similar workable temperature in a remote and localized manner (Fig. 5, E and F). In addition to AuNP-based SMARS droplet modules, various droplet counterparts with similar transportation and separation behaviors are also available by altering the trapping materials, such as GO, Ag, CB, ZIF-67, and TCP (fig. S27). Apart from the droplet, SMARS manifest similar maneuverability irrespective of their geometries, such as SMARS encapsulated in a capillary tube (fig. S23). Moreover, as shown in fig. S28, the solute of the SMARS in the capillary tube can be dynamically formatted into different segments in accordance with applied magnetic fields, and thus leading to a designated redistribution of thermally active region.

I_3^--SMARS enabling TE performance regulation (ionic module)

Given the generality and controllability of the methodology, we construct an ionic module SMARS with I^-/I_3^- redox couple as trapped species (termed I_3^--SMARS). An ionic level control of TE performance is realized by the "separable" trapping and manipulation of the inherent hydrophobic I_3^- parts of I^-/I_3^- that yield a dynamic internal gradient of I_3^-. To quantify the empirical investigations of I_3^--SMARS, we measured the Seebeck coefficient (S_e), expressed in equation $S_e = V_{oc}/\Delta T$, from the open circuit voltage (V_{oc}) induced over I_3^--SMARS by a given temperature gradient (fig. S29). The corresponding S_e for I_3^--SMARS with different pNIPAM concentrations at magnetic field on (*H* on) or off (*H* off) commands is shown in Fig. 6A. Apparently, the I_3^--SMARS invert from p-type (positive S_e) to *n*-type (negative S_e), taking the concentration of pNIPAM at ~1.5 weight % as a demarcation, which is consistent with the previous report (*38*). The S_e is also unprecedentedly modulated by the external magnetic field with attractive force on the hot side of the system, ascribed to the separable trapping and manipulability of I_3^- (inset photographs in Fig. 6A). The voltage profiles, presented in Fig. 6B, indicate I_3^--SMARS on the condition of "*H* on" exhibit superior TE performance relative to its "*H* off" counterpart, evinced by the increased negative V_{oc} (−6.6 mV versus −4.2 mV) at the same ΔT of ~3 K. Moreover, by exerting the magnetic field (*H* on) during the heating process, the transient influence of the magnetic field is further demonstrated, as indicated by the apparent oscillation in Fig. 6C and fig. S30. Besides the controllability of S_e and V_{oc}, as shown in Fig. 6D, the I_3^--SMARS manifest sustained enhancement of TE performance in the presence of the magnetic field with respect to

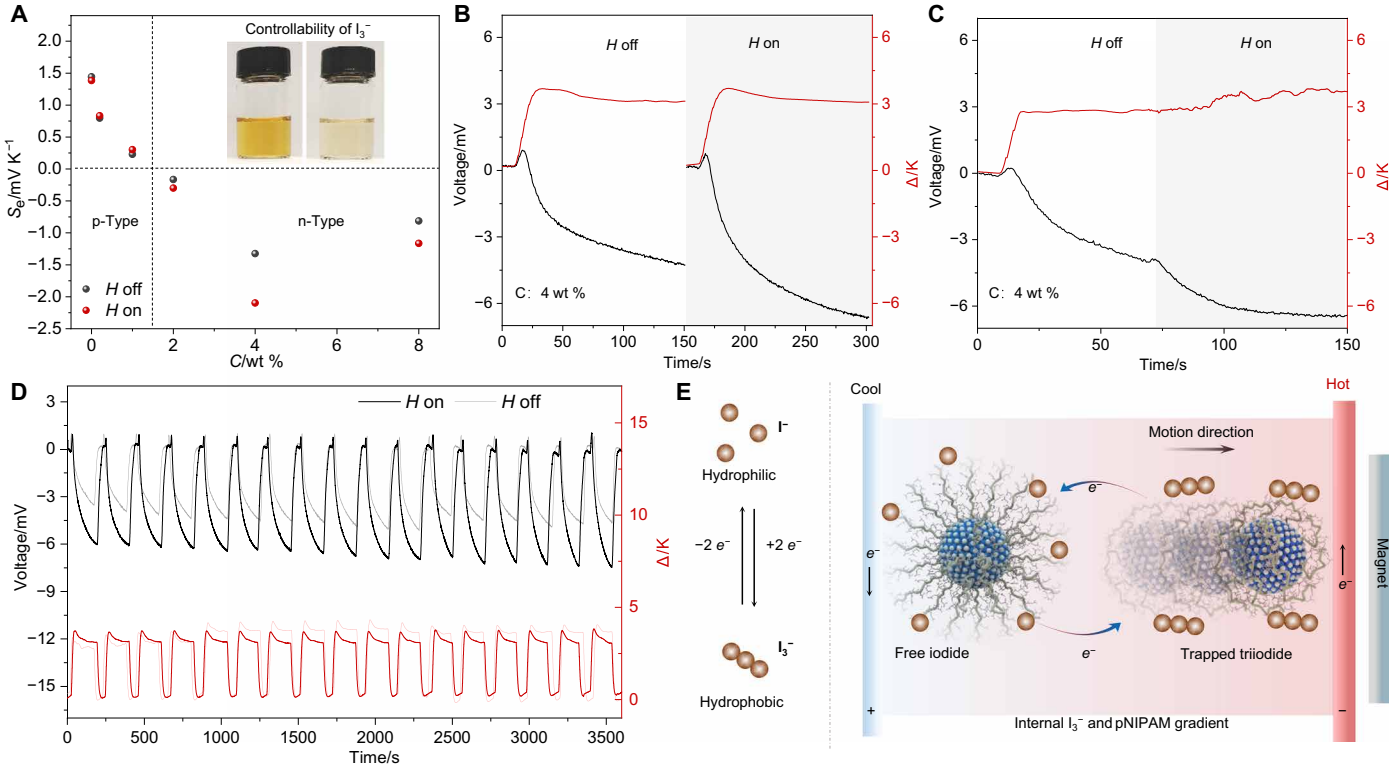

Fig. 6. I_3^--SMARS enabling TE performance regulation (ionic module). (**A**) Comparisons of Seebeck coefficient (S_e) for I_3^--SMARS containing different concentrations of the pNIPAM at the steady state on the condition of *H* on/off. Photographs of the initial I_3^-/I^- electrolytes (left) and control counterpart after trapping and separation (right), indicating the controllability of I_3^- of SMARS. For clarity, the magnet and the magnetic component of SMARS were removed before the photos were taken. (**B**) The dependence of the voltage for I_3^--SMARS with *H* on and off, showing enhanced voltage under magnetic field. (**C**) Voltage profile of exerting magnetic field during heating process, showing the transient controllability of TE performance. (**D**) Stability of the output voltage for I_3^--SMARS with and without magnetic field. (**E**) Proposed mechanism for magnetic control of the internal gradient of I_3^-. Photo credit: Tongtao Li, National University of Singapore.

that of the *H* off control case at a similar ΔT. This indicates a high durability in gaining the control of the internal electrochemical gradient, as opposed to the equilibrium state, by virtue of its intrinsic hydrophobic characteristics. As shown in Fig. 6E, the I_3^--SMARS trap the I_3^- at the hot side of the electrochemical system ($T > T_c$), while it releases I_3^- at the cool side. Under an applied magnetic field, we surmised that the migration of host MNPs creates an internal pNIPAM gradient within the I_3^--SMARS electrolyte and, consequently, induces enlarged I_3^- gradient, thus resulting in enhanced TE performance. Note that the induced internal gradients of I_3^--SMARS are easily administered by both external magnetic and thermal fields, together with the flexibility in tuning active components, which promise previously unidentified opportunities in emerging smart electronics.

DISCUSSION

A considerable challenge in the quest to artificial swarming lies in the dynamic integration of simple, discrete, and dissimilar materials into one high-level dynamic swarm system with desired functionalities. We develop SMARS composed of often deemed discrete and spatially nonaddressable materials, which is switchable by opto/thermal stimulus to gain continuous deterministic locomotion, geometrical topologies, and control authority via ionic/NP-level trapping behaviors and synchronous magnetic maneuverability. Benefiting from the collective merits of fluidic deformability and customized entities, such SMARS manifest intriguing reconfigurability and innumerable possibilities in many areas. (i) SMARS can be easily reconfigured into reversible magneto-plasmonic alignments and their derivatives, or else not easily available complex structures, which promise potential applications in anisotropic material synthesis and corresponding optical/mechanical functions; (ii) chameleon-like SMARS microchains, with controllable color, morphological changes, and magnetic actuation abilities, may act as dynamic microsensor/probe to detect the temperature changes in a confined space; (iii) SMARS vesicles with multiscale reconfigurability and controllable transmittance of SLW can be potentially integrated into a smart mini window to regulate the light/solar characteristics; and (iv) macroscopic SMARS smart droplets capable of long-distance spatial transportation and addressable magnetic "solute/solvent" separation are promising in the realm of water purification in specific microenvironment. I_3^--SMARS are constructed, in which unparalleled separable I_3^- manipulation of the I_3^-/I^- electrolyte is demonstrated, which subsequently exercises a directive influence on the TE properties. Last, given the SMARS flexibility in conforming multiple materials components and structural formats, besides active controllability and reconfigurability, it offers dynamic integral system perspectives composed of customized materials with personalized functionalities, which lends itself to adaptable smart devices and technologies.

MATERIALS AND METHODS

Chemicals

Iron(III) chloride hexahydrate ($FeCl_3{\cdot}6H_2O$, >97%), iron(II) chloride ($FeCl_2$, 98%), $Co(NO_3)_2{\cdot}6H_2O$, sodium citrate dehydrate (Na_3-citrate, ≥99%), gold(III) chloride trihydrate ($HAuCl_4{\cdot}3H_2O$, ≥99.9%), silver nitrate ($AgNO_3$, ≥99.0%), tannic acid (American Chemical Society reagent), hexane (95%), iodine (I_2, >98.0%), potassium iodide (KI, ≥99.5%), pNIPAM carboxylic acid terminated (pNIPAM-COOH, M_n ~ 2000), pNIPAM-amine terminated (pNIPAM-NH_2, M_n ~ 5500), trichloro(1*H*,1*H*,2*H*,2*H*-perfluorooctyl)silane (PFOTCS), tetraethyl orthosilicate (TEOS, 98%), polystyrene-block-poly(ethylene-ran-butylene)-block-polystyrene-graft-maleic anhydride (maleic copolymer), and *N*,*N*-bis(acryloyl)cystamine (BACA) were purchased from Sigma-Aldrich. Acrylamide monomer (AM, >98.0%), ammonium peroxodisulfate (APS, >99.0%), and 2-methylimidazole (2-MIM) were purchased from Tokyo Chemical Industry. Ammonium hydroxide (28 to 30%) was purchased from Acros Organics. All chemicals were used without further purification.

Preparation of host species for SMARS based on a ligand exchange strategy

Preparation of Fe_3O_4 MNPs

In a typical synthesis procedure, 5 ml of mixed aqueous solution of 2.11 g of $FeCl_3{\cdot}6H_2O$ and 0.82 g of $FeCl_2$ was slowly added into 100 ml of ammonia solution (4%) in a 250-ml three-neck flask. The resulting solution was stirred at room temperature (25°C) for 0.5 hour, subsequently heated up to 80°C under N_2, and held at this temperature for 1 hour. After that, 10 ml of Na_3-citrate (0.88 g) aqueous solution was injected and incubated for 0.5 hour before cooling down. MNPs were separated and purified by centrifugation with acetone and deionized (DI) water for two times (*39*). The precipitated MNPs were redispersed in water with a concentration of ~2.5 mg ml^{-1}.

Ligand exchange with thermoresponsive pNIPAM-NH_2 polymer

To construct host MNP species of the SMARS, the as-prepared MNPs were subjected to a solution-phase ligand exchange process using pNIPAM-NH_2 polymer. Typically, 25 mg of pNIPAM-NH_2 was dissolved in 5 ml of freshly prepared MNPs and vigorously stirred at room temperature for 1 hour to incubate the ligand exchange process. Since modified MNPs remain colloidally stable at room temperature, while aggregation occurred upon heating up to its phase transition temperature (above 32°C), the mixed solution was transferred to a 60°C oven to remove the replaced citrate ligand. Then, the pNIPAM-decorated MNPs were readily collected by a magnet, purified by three rounds of phase transition magnetic separation with DI water (5 ml), and redispersed in DI water, giving a concentration of pNIPAM-decorated MNPs of about 7.5 mg ml^{-1}. The area PNIPAM concentration of host MNPs is fixed at ~2.08 nm^{-2}.

Preparation of representative trapped materials for SMARS

pNIPAM-modified AuNPs

Typically, 29.5 mg of $HAuCl_4{\cdot}3H_2O$ was dissolved in 50 ml of DI water in a 250-ml flask and the solution was heated until boiling, then 1 ml of Na_3-citrate (56.5 mg) aqueous solution was injected, and a bright red color reflected from the mixed solution immediately, indicating the successful preparation of AuNPs; the concentration of the AuNPs is ~2 mg ml^{-1}.The different concentrations of the AuNP solutions were prepared by directly increasing the amounts of $HAuCl_4{\cdot}3H_2O$ and Na_3-citrate in the same proportions (*40*). To realize pNIPAM-decorated AuNPs, 2.5 mg of pNIPAM-NH_2 was dissolved in 1 ml of DI water and mixed with 50 ml of freshly prepared AuNPs and vigorously stirred at room temperature for 1 hour to incubate the ligand exchange process. The area PNIPAM concentration of AuNPs is about 0.13 nm^{-2}. By simply tuning the relative ratio of pNIPAM and AuNPs, pNIPAM-decorated AuNPs with different surface concentrations of pNIPAM can be obtained, such as ψ = 0.02 and 2.6 nm^{-2}.

pNIPAM-decorated AgNPs

A total of 147 mg of Na_3-citrate and 4.2 mg of tannic acid were dissolved in 100 ml of DI water in a 250-ml flask, and the solution was heated until boiling; then, 1 ml of $AgNO_3$ (42 mg) aqueous solution was injected, and a bright yellow color reflected from the mixed solution immediately, indicating the successful preparation of AgNPs. The different concentrations of the AgNP solutions were prepared by directly increasing the amounts of $AgNO_3$ and Na_3-citrate in the same proportions. The grafting and ligand exchange process of AgNPs were conducted similarly to their AuNP counterparts.

pNIPAM-decorated GO

GO was synthesized by a modified Hummers process (*23*). The grafting and ligand exchange process of GO were conducted similarly to its AuNP counterparts.

Thermochromic pigments

A total of 0.5 mg of commercial TCPs was dissolved in 5 ml of DI water and ultrasonically treated for 30 min. After naturally precipitating for 6 hours, the super-suspension of TCPs was collected for further use without any other treatment.

Triodide/iodide redox couple (I^-/I_3^-)

A total of 83 mg of KI and 64 mg of I_2 were dissolved in 50 ml of DI water for further use without any other treatment.

Zeolitic imidazolate framework-67

Two solutions were prepared separately by dissolving 2.91 g of $Co(NO_3)_2{\cdot}6H_2O$ and 3.28 g of 2-MIM in 200 ml of methanol. Then, 2-MIM solution was quickly added into a cobalt nitrate solution and mixed under vigorous stirring and aged at room temperature for 24 hours. The precipitate was collected by centrifugation, washed with methanol, and dried.

Construction of customized SMARS

Take AuNP trapped SMARS as an example, SMARS containing MNPs ($2.08/nm^2$) and AuNPs ($0.13/nm^2$), with a particle mass ratio of MNPs:AuNPs ≈ 1:20, were prepared by mixing 0.4 ml of host pNIPAM-decorated MNP and 10 ml of pNIPAM-decorated AuNP solutions. The SMARS were always matured by several rounds of heating up (60°C) and cooling down (25°C). Attributing to the flexibility of the method, SMARS with other trapped entities, such as Ag, GO, Zif-67, TCPs, and I^-/I_3^-, can be readily constructed similarly to AuNP trapped counterparts.

Construction of SMARS microchains by nanoscale conformal encapsulation.

Typically, 1 ml of SMARS was heated up to 60°C in oven within a uniform magnetic field, and then 30 μl of BAC (4 mg ml^{-1}) was added. After 10 min, 30 μl of AM (0.5 g ml^{-1}) and 10 μl of APS (0.1 g ml^{-1}) were successively added and incubated for 3 hours. The prepared SMARS microchains can be readily extracted by a magnet and redispersed into DI water while retaining its microscale chain-like structure. For the preparation of L-shape chains, when heated up to 60°C, SMARS was first subjected to an *x* axis uniform magnetic field, which enabled the formation of *x* axis alignment. After partial sedimentation of the alignment caused by gravity for ~10 min, the *x* axis magnetic field was removed, and a *y* axis uniform magnetic field was simultaneously exerted. The encapsulation process was conducted similarly to their linear chain counterparts.

Construction of SMARS vesicles by emulsifying SMARS

Typically, 15 mg of maleic copolymer was thoroughly dissolved in 2 ml of hexane, and then 0.5 ml of SMARS solution was added dropwise. The biphase mixture was further agitated by a vortex mixer for 10 s to yield SMARS vesicles dispersed in hexane, which can remain stable for at least 1 month.

Fabrication of superhydrophobic surface

First, the substrates (glass slide and beaker) were coated with candle soot, and then a silica shell was synthesized by chemical vapor deposition and, subsequently, hydrolysis and condensation process of 2 ml of TEOS for 20 hours in a sealed environment that contained 2 ml of ammonia solution. After that, the carbon constituent of the coating was removed by annealing at 550°C in air for 3 hours and subjected to oxygen plasma treatment for 10 min. After that, the superhydrophobic surface can be prepared by a chemical vapor deposition modification with PFOTCS in a sealed environment for at least 2 hours (*17*).

Characterization techniques

The optical images were monitored with an Olympus BX53M microscope in bright-field mode, equipped with a homemade temperature/magnetic dual-controlled microscope stage. Field emission SEM and elemental analysis were performed on a JEOL FEG JSM-7001F microscope equipped with an Oxford/INCA EDS. Transmission electron microscopy (TEM) images were obtained using a JEOL JEM-2010F microscope. Fourier transform infrared spectroscopy spectrum was collected on a Shimadzu IR Prestige-21 spectrophotometer. Ultraviolet-visible (UV-vis) absorption spectra were recorded on a Shimadzu UV-3600 UV-vis near-infrared spectrophotometer. X-ray diffraction was carried out on a Bruker D4 X-ray diffractometer. AFM images were collected on a commercial scanning probe microscope (SPM) instrument (MFP-3D, Asylum Research, CA, USA). The temperature and open-circuit voltage of I_3^--SMARS were recorded on a nanovoltmeter (Keithley 2182A). The infrared camera was used to capture infrared image and surface temperature. Simulated sunlight with a radiation intensity of 5 kW m^{-2} was provided by a 300-W Xenon lamp (Excelitas, PE300BFM).

SUPPLEMENTARY MATERIALS

Supplementary material for this article is available at http://advances.sciencemag.org/cgi/content/full/7/2/eabe3184/DC1

REFERENCES AND NOTES

1. M. Rubenstein, A. Cornejo, R. Nagpal, Programmable self-assembly in a thousand-robot swarm. *Science* **345**, 795–799 (2014).
2. A. Kaiser, A. Snezhko, I. S. Aranson, Flocking ferromagnetic colloids. *Sci. Adv.* **3**, e1601469 (2017).
3. Y. Yang, M. A. Bevan, Cargo capture and transport by colloidal swarms. *Sci. Adv.* **6**, eaay7679 (2020).
4. J. Yu, D. Jin, K.-F. Chan, Q. Wang, K. Yuan, L. Zhang, Active generation and magnetic actuation of microrobotic swarms in bio-fluids. *Nat. Commun.* **10**, 5631 (2019).
5. S. Ghosh, A. Ghosh, All optical dynamic nanomanipulation with active colloidal tweezers. *Nat. Commun.* **10**, 4191 (2019).
6. J. Li, B. Esteban-Fernandez de Avila, W. Gao, L. Zhang, J. Wang, Micro/nanorobots for biomedicine: Delivery, surgery, sensing, and detoxification. *Sci. Robot.* **2**, eaam6431 (2017).
7. J.-a. Lv, Y. Liu, J. Wei, E. Chen, L. Qin, Y. Yu, Photocontrol of fluid slugs in liquid crystal polymer microactuators. *Nature* **537**, 179–184 (2016).
8. W. Hu, G. Z. Lum, M. Mastrangeli, M. Sitti, Small-scale soft-bodied robot with multimodal locomotion. *Nature* **554**, 81–85 (2018).
9. Z. Yang, J. Wei, Y. I. Sobolev, B. A. Grzybowski, Systems of mechanized and reactive droplets powered by multi-responsive surfactants. *Nature* **553**, 313–318 (2018).
10. O. M. Marago, P. H. Jones, P. G. Gucciardi, G. Volpe, A. C. Ferrari, Optical trapping and manipulation of nanostructures. *Nat. Nanotechnol.* **8**, 807–819 (2013).

11. U. G. Butaite, G. M. Gibson, Y. D. Ho, M. Taverne, J. M. Taylor, D. B. Phillips, Indirect optical trapping using light driven micro-rotors for reconfigurable hydrodynamic manipulation. *Nat. Commun.* **10**, 1215 (2019).
12. A. Dong, J. Chen, P. M. Vora, J. M. Kikkawa, C. B. Murray, Binary nanocrystal superlattice membranes self-assembled at the liquid-air interface. *Nature* **466**, 474–477 (2010).
13. M. A. Boles, M. Engel, D. V. Talapin, Self-assembly of colloidal nanocrystals: From intricate structures to functional materials. *Chem. Rev.* **116**, 11220–11289 (2016).
14. T. Li, B. Wang, J. Ning, W. Li, G. Guo, D. Han, B. Xue, J. Zou, G. Wu, Y. Yang, A. Dong, D. Zhao, Self-assembled nanoparticle supertubes as robust platform for revealing long-term, multiscale lithiation evolution. *Matter* **1**, 976–987 (2019).
15. B. Bharti, A. L. Fameau, M. Rubinstein, O. D. Velev, Nanocapillarity-mediated magnetic assembly of nanoparticles into ultraflexible filaments and reconfigurable networks. *Nat. Mater.* **14**, 1104–1109 (2015).
16. L. Lin, J. Zhang, X. Peng, Z. Wu, A. C. H. Coughlan, Z. Mao, M. A. Bevan, Y. Zheng, Opto-thermophoretic assembly of colloidal matter. *Sci. Adv.* **3**, e1700458 (2017).
17. Q. Sun, D. Wang, Y. Li, J. Zhang, S. Ye, J. Cui, L. Chen, Z. Wang, H. J. Butt, D. Vollmer, X. Deng, Surface charge printing for programmed droplet transport. *Nat. Mater.* **18**, 936–941 (2019).
18. Y. Chen, Z. Wang, Y. He, Y. J. Yoon, J. Jung, G. Zhang, Z. Lin, Light-enabled reversible self-assembly and tunable optical properties of stable hairy nanoparticles. *Proc. Natl. Acad. Sci. U.S.A.* **115**, E1391–E1400 (2018).
19. Q. Cao, Q. Fan, Q. Chen, C. Liu, X. Han, L. Li, Recent advances in manipulation of micro-and nano-objects with magnetic fields at small scales. *Mater. Horiz.* **7**, 638–666 (2020).
20. Z. Li, F. Yang, Y. Yin, Smart materials by nanoscale magnetic assembly. *Adv. Funct. Mater.* **30**, 1903467 (2020).
21. W. Wang, J. V. I. Timonen, A. Carlson, D. M. Drotlef, C. T. Zhang, S. Kolle, A. Grinthal, T. S. Wong, B. Hatton, S. H. Kang, S. Kennedy, J. Chi, R. T. Blough, M. Sitti, L. Mahadevan, J. Aizenberg, Multifunctional ferrofluid-infused surfaces with reconfigurable multiscale topography. *Nature* **559**, 77–82 (2018).
22. H. Xie, M. Sun, X. Fan, Z. Lin, W. Chen, L. Wang, L. Dong, Q. He, Reconfigurable magnetic microrobot swarm: Multimode transformation, locomotion, and manipulation. *Sci. Robot.* **4**, eaav8006 (2019).
23. P. Zhang, F. Liu, Q. Liao, H. Yao, H. Geng, H. Cheng, C. Li, L. Qu, A microstructured graphene/poly (N-isopropylacrylamide) membrane for intelligent solar water evaporation. *Angew. Chem. Int. Ed.* **57**, 16343–16347 (2018).
24. L. Lin, E. H. Hill, X. Peng, Y. Zheng, Optothermal manipulations of colloidal Particles and living cells. *Acc. Chem. Res.* **51**, 1465–1474 (2018).
25. Y. Ke, C. Zhou, Y. Zhou, S. Wang, S. H. Chan, Y. Long, Emerging thermal-responsive materials and integrated techniques targeting the energy-efficient smart window application. *Adv. Funct. Mater.* **28**, 1800113 (2018).
26. X.-H. Li, C. Liu, S.-P. Feng, N. X. Fang, Broadband light management with thermochromic hydrogel microparticles for smart windows. *Jouele* **3**, 290–302 (2019).
27. Y. Cheng, K. H. Chan, X. Q. Wang, T. Ding, T. Li, X. Lu, G. W. Ho, Direct-ink-write 3D printing of hydrogels into biomimetic soft robots. *ACS Nano* **13**, 13176–13184 (2019).
28. T. Ding, V. K. Valev, A. R. Salmon, C. J. Forman, S. K. Smoukov, O. A. Scherman, D. Frenkel, J. J. Baumberg, Light-induced actuating nanotransducers. *Proc. Natl. Acad. Sci. U.S.A.* **113**, 5503–5507 (2016).
29. H. Han, J. Y. Lee, X. Lu, Thermoresponsive nanoparticles + plasmonic nanoparticles = photoresponsive heterodimers: Facile synthesis and sunlight-induced reversible clustering. *Chem. Commun.* **49**, 6122–6124 (2013).
30. J. J. Lai, J. M. Hoffman, M. Ebara, A. S. Hoffman, C. Estournes, A. Wattiaux, P. S. Stayton, Dual magnetic–/temperature-responsive nanoparticles for microfluidic separations and assays. *Langmuir* **23**, 7385–7391 (2007).
31. J. Shen, B. Luan, H. Pei, Z. Yang, X. Zuo, G. Liu, J. Shi, L. Wang, R. Zhou, W. Cheng, C. Fan, Humidity-responsive single-nanoparticle-layer plasmonic films. *Adv. Mater.* **29**, (2017).
32. M. Kalaj, K. C. Bentz, S. Ayala Jr., J. M. Palomba, K. S. Barcus, Y. Katayama, S. M. Cohen, MOF-polymer hybrid materials: From simple composites to tailored architectures. *Chem. Rev.* **120**, 8267–8302 (2020).
33. K. C.-F. Leung, S. Xuan, X. Zhu, D. Wang, C.-P. Chak, S.-F. Lee, W. K.-W. Ho, B. C.-T. Chung, Gold and iron oxide hybrid nanocomposite materials. *Chem. Soc. Rev.* **41**, 1911–1928 (2012).
34. C. Yu, J. Fan, B. Tian, D. Zhao, Morphology development of mesoporous materials: A colloidal phase separation mechanism. *Chem. Mater.* **16**, 889–898 (2004).
35. J. V. Timonen, M. Latikka, L. Leibler, R. H. Ras, O. Ikkala, Switchable static and dynamic self-assembly of magnetic droplets on superhydrophobic surfaces. *Science* **341**, 253–257 (2013).
36. P. Aussillous, D. Quere, Liquid marbles. *Nature* **411**, 924–927 (2001).
37. A. Li, H. Li, Z. Li, Z. Zhao, K. Li, M. Li, Y. Song, Programmable droplet manipulation by a magnetic-actuated robot. *Sci. Adv.* **6**, eaay5808 (2020).
38. J. Duan, B. Yu, K. Liu, J. Li, P. Yang, W. Xie, G. Xue, R. Liu, H. Wang, J. Zhou, P-N conversion in thermogalvanic cells induced by thermo-sensitive nanogels for body heat harvesting. *Nano Energy* **57**, 473–479 (2019).
39. T. Fried, G. Shemer, G. Markovich, Ordered two-dimensional arrays of ferrite nanoparticles. *Adv. Mater.* **13**, 1158–1161 (2001).
40. H. Qin, T. Zhang, H.-N. Li, H.-P. Cong, M. Antonietti, S.-H. Yu, Dynamic Au-thiolate interaction induced rapid self-Healing nanocomposite hydrogels with remarkable mechanical behaviors. *Chem* **3**, 691–705 (2017).

Acknowledgments

Funding: This research is supported by the Ministry of Education, Singapore, under its Academic Research Fund Tier 2 (award MOE2017-T2-2-102) and NUS Hybrid Integrated Flexible (Stretchable) Electronic Systems Program grant number R-263-501-011-731. **Author contributions:** T.L. conceived the idea, conducted the experiments, and wrote the paper. K.H.C. assembled the temperature/magnetic dual-controlled microscope stage and assisted in taking pictures and movies. T.D. directed the characterization of TE performance and helped in data analysis. X.-Q.W., Y.C., and C.Z. helped improve the idea and assisted in the experiments. W.L. performed the AFM experiments. G.Y. performed the TEM experiments. C.-W.Q. helped with the data analysis and manuscript preparation. G.W.H. supervised the project, conceived the idea, and wrote the paper. All authors discussed the results and commented on the manuscript. **Competing interests:** The authors declare that they have no competing interests. **Data and materials availability:** All data needed to evaluate the conclusions in the paper are present in the paper and/or the Supplementary Materials. Additional data related to this paper may be requested from the authors. Source data for movies S1 to S10 are available with the paper.

Submitted 14 August 2020
Accepted 13 November 2020
Published 6 January 2021
10.1126/sciadv.abe3184

Citation: T. Li, K. H. Chan, T. Ding, X.-Q. Wang, Y. Cheng, C. Zhang, W. Lu, G. Yilmaz, C.-W. Qiu, G. W. Ho, Dynamic thermal trapping enables cross-species smart nanoparticle swarms. *Sci. Adv.* **7**, eabe3184 (2021).